LANGMUIR

pubs.acs.org/Langmuir Article

Thermodynamic Insights into Anoxic Arsenic(III) Oxidation: The Critical Role of Oxygen Vacancies in Regulating Redox Reactivity of Fe(II) Bound to Fe(III) (Oxyhydr)oxide Redox Couples

Juan Liu, Jingtao Hou,* Siyuan Zheng, Juan Xiong, Mingxia Wang, Andreas Kappler, and Wenfeng Tan

Cite This: *Langmuir* 2026, 42, 19343−19353 Read Online

ACCESS | Metrics & More | Article Recommendations | Supporting Information

ABSTRACT: Ferrous iron (Fe(II)) bound to Fe(III) minerals redox couples are ubiquitous in sediments and groundwater, playing a crucial role in arsenic migration, transformation, and associated risks. Although Fe(III) oxides−Fe(II) couples are well known for their reductive transformation of pollutants, the thermodynamic mechanisms driving anoxic As(III) oxidation observed in these systems remain poorly understood. In this study, we combined high-resolution transmission electron microscopy−selected area electron diffraction mapping, Mössbauer spectroscopy, and density functional theory calculations to investigate whether anoxic As(III) oxidation in hematite−Fe(II) couples is influenced by oxygen vacancies (Ov), an intrinsic characteristic of iron (oxyhydr)oxide minerals. Batch experiments demonstrated that Ov in hematite significantly enhanced the As(III) oxidation efficiency (62.7%) compared to defect-free hematite (45.9%) at pH 6 with 0.2 mM Fe(II). Spectroscopic and microscopic analyses revealed recrystallization processes that generated active metastable iron phases after Fe(II) adsorption, acting as electron acceptors for As(III) oxidation. Notably, the defective hematite−Fe(II) couples generated a higher content of active iron phase compared to their defect-free counterparts, which was attributed to thermodynamically favorable electron transfer between Fe(II) and the defective hematite due to the relatively higher redox potential of defective hematite (E_H^0 = +1297 mV *vs* +670 mV). These findings provide evidence of the thermodynamically driven anoxic transformation of As(III), emphasizing the critical role of oxygen vacancies in regulating redox reactivity in oxide-Fe(II) systems.

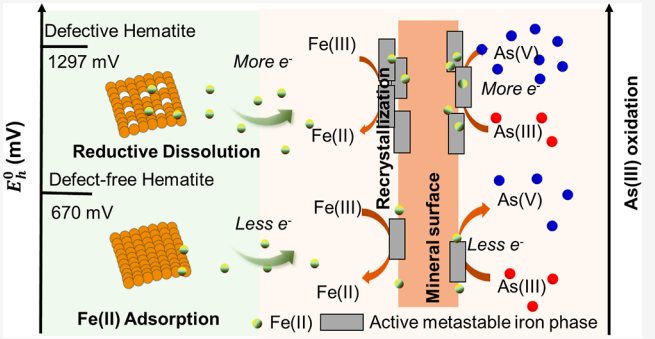

1. INTRODUCTION

Arsenic (As), a metalloid known for its high carcinogenicity and toxicity, is primarily released through geological processes (e.g., weathering of As-bearing Fe(III) (oxyhydr)oxides) and anthropogenic activities (e.g., mining, smelting, and the use of arsenical pesticides), leading to significant environmental pollution.[1] The environmental behavior of As is largely determined by its chemical speciation, which directly influences its bioavailability and mobility.[2] Among its species, arsenite (As(III)) is more toxic than arsenate (As(V)). The oxidation transformation of As(III) to As(V) therefore is considered a key detoxification pathway that also promotes arsenic immobilization. However, under anoxic conditions, microbial reduction of As(V) back to As(III) enhances arsenic mobility and toxicity, thereby posing elevated environmental and health risks.[3] A comprehensive understanding of arsenic transformation pathways is critical for accurately predicting its environmental fate and for developing effective mitigation strategies.

Iron (Fe), the fourth most abundant element in the Earth's crust, constitutes approximately 4.75% of the Earth's crustal composition and is widely distributed across soils, water, and living organisms.[4] Iron (oxyhydr)oxides, commonly coating soil particles and colloidal surfaces, exhibit reactivity far exceeding their relative abundance, making them a crucial component in soil and sediment systems.[5] However, under anoxic conditions, iron oxides can act as electron acceptors to be reduced by dissimilatory iron(III)-reducing bacteria, which release ferrous iron (Fe(II)) species from the mineral structure. These Fe(II) species can adsorb onto the surface of Fe(III) minerals, forming specific Fe(III) oxide−Fe(II) redox couples, which show significantly higher reduction rates for oxidized pollutants than aqueous Fe(II) (Fe_{aq}^{2+}) alone. For example, Stewart et al. demonstrated that Fe(II)-goethite rapidly reduces nitrobenzene, linking its reduction to electron

Received: April 24, 2026
Revised: June 10, 2026
Accepted: June 11, 2026
Published: June 23, 2026

Downloaded from pubs.acs.org/langd5/article-pdf/42/26/19343/6521356l/acs.langmuir.6c02392.pdf by UNIV TUEBINGEN user on 17 September 2026

© 2026 American Chemical Society

https://doi.org/10.1021/acs.langmuir.6c02392
Langmuir 2026, 42, 19343−19353

transfer within the iron oxide structure under anoxic conditions.[6] Similarly, Li et al. reported that Fe(II)-ferrihydrite reduces anthraquinone-2,6-disulfonate (AQDS) under anoxic conditions.[7] The enhanced reduction ability of Fe(II) in the presence of minerals was also observed to drive the transformation of As(V) to As(III), which significantly affects the mobility and toxicity of As species. In contrast to As(V) reduction, some researchers observed the oxidation behavior of As(III) to As(V) by Fe(II)−Fe(III) oxide couples, although it is widely accepted that this process is thermodynamically unfavorable.[8,9] The underlying mechanisms that determine why As(V) reduction can appear in some Fe(II)−Fe(III) oxide systems, while other Fe(II)−Fe(III) oxide couples show As(III) oxidation, are still a puzzling and not fully understood question.

In principle, the discrepancy in the redox behavior of As on Fe(II)−Fe(III) oxide couples may arise from variations in the surface properties of the iron minerals, which are determined by their surface structure. Recent studies have shown that the presence of Fe vacancy defects in Fe(III) oxyhydroxides (e.g., goethite) can accelerate the electron transfer between structural Fe(III) and surface-bound Fe(II), which is attributed to the relatively lower surface energy of defective minerals compared to their defect-free counterparts.[10] Building on this, Fang and coworkers demonstrated that Fe vacancies in goethite significantly facilitate the oxidation of As(III) by the Fe(II)-goethite redox couple under anoxic conditions.[11] These findings suggest that surface defects in iron minerals play a critical role in affecting the As redox pathways in Fe(III) oxide-Fe(II) redox systems. Remarkably, defects in iron minerals often exist in the form of iron or oxygen vacancy. For instance, the defect type in the hematite (α-Fe_2O_3) structure can be identified by deviations in its atomic stoichiometry (α-$Fe_{2-y}O_{3-x}$) relative to its theoretical formula. In iron oxides, oxygen atoms occupy the outer spheres of Fe−O octahedral units, with each Fe atom typically surrounded by six oxygen atoms. In this configuration, the release of a single Fe atom, often mediated by dissimilatory Fe(III)-reducing bacteria (e.g., *Shewanella* spp.), can result in the formation of two or more oxygen vacancies at the mineral surface. Therefore, oxygen vacancy defects are generally more likely to form compared to Fe vacancies in naturally occurring iron minerals. However, there is currently a lack of thermodynamic evidence to confirm whether oxygen vacancies actively drive the oxidation of As(III) by Fe(III) oxides−Fe(II) redox couples.

Herein, our study focuses on hematite, a thermodynamically stable Fe(III) oxide known for its high reactivity and widespread occurrence in natural environments. To simulate the reductive dissolution of hematite, we employed sodium borohydride ($NaBH_4$) as a chemical reductant to generate oxygen vacancy defects on the surfaces of hematite. The objectives of this work are (1) to assess the extent to which oxygen vacancies influence As(III) oxidation by an Fe(III) oxide−Fe(II) redox couple; (2) to investigate the electron transfer behavior of a defective Fe(III) oxide−Fe(II) redox couple; and (3) to elucidate the underlying thermodynamic mechanisms of anoxic As(III) oxidation in these systems.

2. MATERIALS AND METHODS

2.1. Mineral Synthesis and Characterization

The synthesis procedures and bulk characterization methods of the defect-free hematite (denoted as Hem) and defective hematite samples (denoted as DHem) used in this study are identical to those described in our previous work.[12] The structure and morphologies of Hem and DHem samples were initially characterized using X-ray diffraction (XRD), scanning electron microscopy (SEM), and transmission electron microscopy (TEM). Both Hem and DHem matched well with the standard diffraction pattern of hematite (JCPDS no. 33-0664) (Figure S1a), and DHem showed a poorer crystallinity after reduction by sodium borohydride ($NaBH_4$). SEM and TEM images exhibited granular morphologies for both samples, while DHem particles showed smaller sizes and more irregular edges (Figure S1b). High-resolution TEM images showed a lattice fringe spacing of 0.373 nm, corresponding to the exposed (012) facet (Figure S1b3−b6). In addition, oxygen vacancy defects were characterized qualitatively and quantitatively using electron paramagnetic resonance (EPR) spectra (Figure S1c) and thermogravimetry−mass spectrometry (TG−MS) (Figure S1d,e). Based on the TG−MS data, the calculated oxygen vacancy concentration of DHem (α-Fe_2O_{3-x}, where x is the fraction of the oxygen vacancy defect) was 3.24 mmol g^{-1}. Finally, the obtained x value in defective hematite is 0.5178. Additionally, high-resolution TEM (HRTEM) combined with selected area electron diffraction (SAED) mapping and Mössbauer spectral studies were conducted to observe the Fe phase evolution of hematite before and after Fe(II) addition. More details of sample preparation and mineral characterization are provided in Texts S1 and S2 and in our previous publication.[12]

2.2. Arsenic Oxidation Experiments

The As(III) oxidation experiments were conducted in the anoxic glovebox to prevent exposure to oxygen. All solutions were purged with dinitrogen gas for 2 h and subsequently transferred into the glovebox to maintain an oxygen-free environment. The experiments were performed at three pH values of 5.0, 6.0, and 7.0 using 25 mM MES (pH 5.0) or MOPS (pH 6.0 and 7.0) as buffers, with 25 mM KCl as the background electrolyte. Varying amounts of the Fe(II) stock solution (prepared from $FeCl_2$ in 1 M HCl) were added to achieve final Fe(II) concentrations of 0.2−5.0 mM. The pH was adjusted to the target value, followed by the addition of preweighed hematite solids to achieve a mineral concentration of 1.0 g L^{-1}, and the mixture was stirred vigorously in the dark for 1 h to allow Fe(II) equilibration with the mineral surface. After equilibration, the pH was verified and adjusted again if necessary. Subsequently, the As(III) stock solution was added to achieve a final As(III) concentration of 100 μM, and the reaction proceeded for 4 h under continuous stirring in the dark.

Dissolved Fe(II) was quantified after filtering through a 0.45 μm nylon syringe filter, while adsorbed Fe(II) was calculated as the difference between total Fe(II) (extracted with 0.5 M HCl for 24 h) and dissolved Fe(II). Fe(II) concentrations were determined via phenanthroline spectrophotometry.[13] Arsenic speciation in solution was analyzed by liquid chromatography−atomic fluorescence spectrometry (LC-AFS) after filtering through a 0.22 μm filter. Surface-associated arsenic (As(III)/As(V)), including adsorbed species on the solid surface, was extracted using a 1 M NaH_2PO_4 solution, shaken at 80 rpm for 24 h. All experiments were conducted in triplicate to ensure the reliability of the results. More details are shown in Text S3.

2.3. Oxidation−Reduction Potential (E_H) Measurements

The E_H values of hematite suspensions were measured using a mediated potentiometric method.[14,15] A 907 Titrando automatic potentiometric titrator equipped with a 6.0451.100 platinum-ring combined redox electrode (Metrohm) was used for the measurements. The experiments were conducted at five Fe(II) concentrations ($FeCl_2$, 0.1∼5.0 mM) and three pH values (5.0, 6.0, and 7.0). Specifically, a 15 mL aqueous solution containing 25 mM KCl was mixed with Fe(II) stock solutions under vigorous agitation. The solution pH was adjusted to the target experimental value. The hematite solid was subsequently added to achieve a final mineral concentration of 1.0 g L^{-1}. A 10 mM $Ru(NH_3)_6$ stock solution was introduced to achieve a final concentration of 20 μM. The pH was readjusted to the initial value. The resulting suspensions were

Downloaded from pubs.acs.org/langd5/article-pdf/42/26/19343/6521356l/acs.langmuir.6c02392.pdf by UNIV TUEBINGEN user on 17 September 2026

https://doi.org/10.1021/acs.langmuir.6c02392
Langmuir 2026, 42, 19343−19353

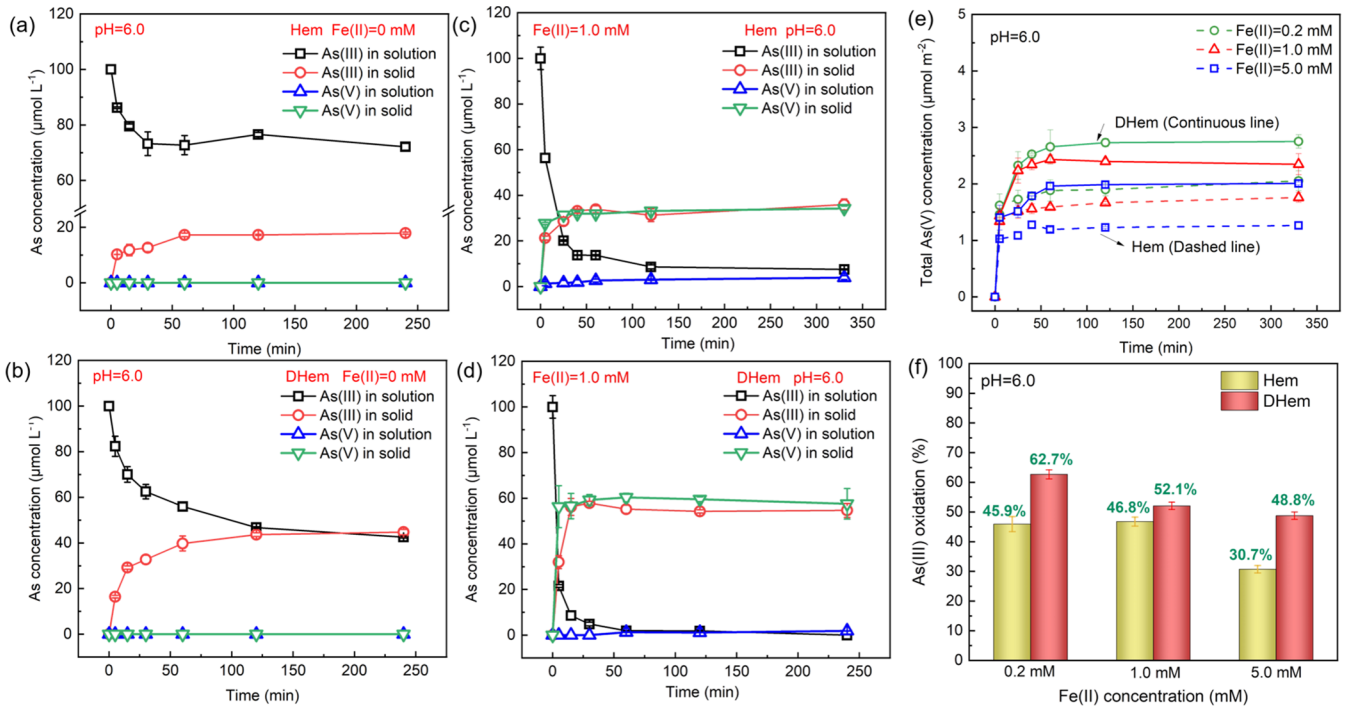

Figure 1. Temporal evolution of As(III) and As(V) concentrations (total As(III) 100 μM) for Hem and DHem samples (1.0 g L^{-1}) in the absence (a,b) and presence of 1.0 mM Fe(II) (c,d) under anoxic conditions at pH = 6.0; the total As(V) concentration and the As(III) oxidation rate in the presence of Fe(II) (0.2, 1.0, and 5.0 mM) at pH = 6.0 (e,f).

equilibrated in the dark under continuous stirring for 24 h. The filtrate was subsequently analyzed to quantify the final concentration of aqueous Fe^{2+} ($Fe^{2+}_{(aq)}$).

Additionally, the Pt-ring combined redox electrode was periodically immersed in 0.1 M HCl for 5 min to remove adsorbed substances and the oxide film on its surface. Subsequently, the electrode was immersed in 3 M KCl for 5 min to recover the diluted reference solution concentration. The electrode was calibrated using a 20 mL buffer solution saturated with 0.1 g of quinone (≥97%, Thermo Scientific) at pH 4.0 and 7.0, yielding calibration values of 265 ± 15 mV and 86 ± 15 mV, respectively. E_H values of the suspensions were measured using a Pt-ring combined redox electrode with a Ag/AgCl as the reference electrode inside the glovebox. The final stable potential measurement was recorded as the E_H value of the suspension.

2.4. Electrochemical Measurements

Cyclic voltammetry (CV) curves were obtained using a CHI660E electrochemical workstation (Shanghai Chenhua Instrument Co., Ltd.). The three-electrode system consisted of an Ag/AgCl electrode, a Pt rod electrode, and a hematite powder-loaded glassy carbon electrode (2 mm diameter) as a reference electrode, counter electrode, and working electrode, respectively. All electrochemical tests were performed under anoxic conditions. The electrolyte solution was maintained at pH 6.0 using 25 mM MOPS and contained 25 mM KCl along with varying concentrations of Fe(II) (0–5 mM). A 5 mg hematite sample was dispersed by vortex mixing in a solution of Nafion (0.5 wt %, 50 μL) diluted with ethanol for 1 min. Subsequently, 2 μL of the resulting suspension was coated onto a clean glassy carbon electrode using a microsyringe, and the electrode was air-dried for 5 min prior to immersion in the anoxic solution. Additionally, cyclic voltammetry curves were recorded at scan rates ranging from 0.01 to 1 V s^{-1}. The relationships between the peak potential shift (E_p–E_0) and the logarithm of the scan rate [log(ν)], as well as between the anodic peak current (i_{pa}) and the square root of the scan rate ($\nu^{0.5}$), were analyzed to elucidate the electrochemical behavior of the system.

2.5. Density Functional Theory Calculations

Density functional theory (DFT) calculations were employed within the generalized gradient approximation (GGA) using the Perdew–Burke–Ernzerhof (PBE) formulation.[16,17] The projected augmented wave (PAW) potentials were employed to describe the ionic cores, while valence electrons were treated using a plane-wave basis set with a kinetic energy cutoff of 450 eV.[16,18,19] An implicit solvation model (H_2O) was used to study the effect of electrostatics, cavitation, and dispersion on solute–solvent interaction including tuning VASP sol parameters. The hydrated Fe(II) was set by surrounding a Fe atom with a −OH group and three H_2O (i.e., $Fe(OH)(OH_2)_3$).[20] Partial occupancies of the Kohn–Sham orbitals were allowed using the Gaussian smearing method with a width of 0.05 eV. Electronic self-consistency was achieved when the total energy change between iterations was less than 10^{-5} eV. Geometry optimizations were considered converged when the forces were below 0.05 eV $Å^{-1}$. A vacuum layer of 18 Å was applied perpendicular to the slab to avoid spurious interactions. The Brillouin zone integration was performed using 2 × 2 × 1 Monkhorst–Pack k-point sampling for a structure. Finally, the adsorption energies (E_{ads}) were calculated as $E_{ads} = E_{ad/sub} - E_{ad} - E_{sub}$, where $E_{ad/sub}$, E_{ad}, and E_{sub} are the total energies of the optimized adsorbate/substrate system, the adsorbate in the structure, and the clean substrate, respectively.

3. RESULTS AND DISCUSSION

3.1. Anoxic As(III) Oxidation Coupled to Fe(III) Reduction on Hematite–Fe(II) Redox Couples

Figure 1a,b illustrates the evolution of As(III) and As(V) species concentration in Hem and DHem without the Fe(II) system. No As(V) species were detected in the solution and on the surface of Hem/DHem samples at pH 6.0, indicating that As(III) oxidation did not occur by the Fe(III) oxide alone, which is in agreement with previous reports.[9] It is reported that direct oxidation of As(III) by lattice Fe(III) is thermodynamically unfavorable under circumneutral and anoxic conditions due to the octahedral coordination and electronic localization

Downloaded from pubs.acs.org/langd5/article-pdf/42/26/19343/6521356l/acs.langmuir.6c02392.pdf by UNIV TUEBINGEN user on 17 September 2026

https://doi.org/10.1021/acs.langmuir.6c02392
Langmuir 2026, 42, 19343–19353

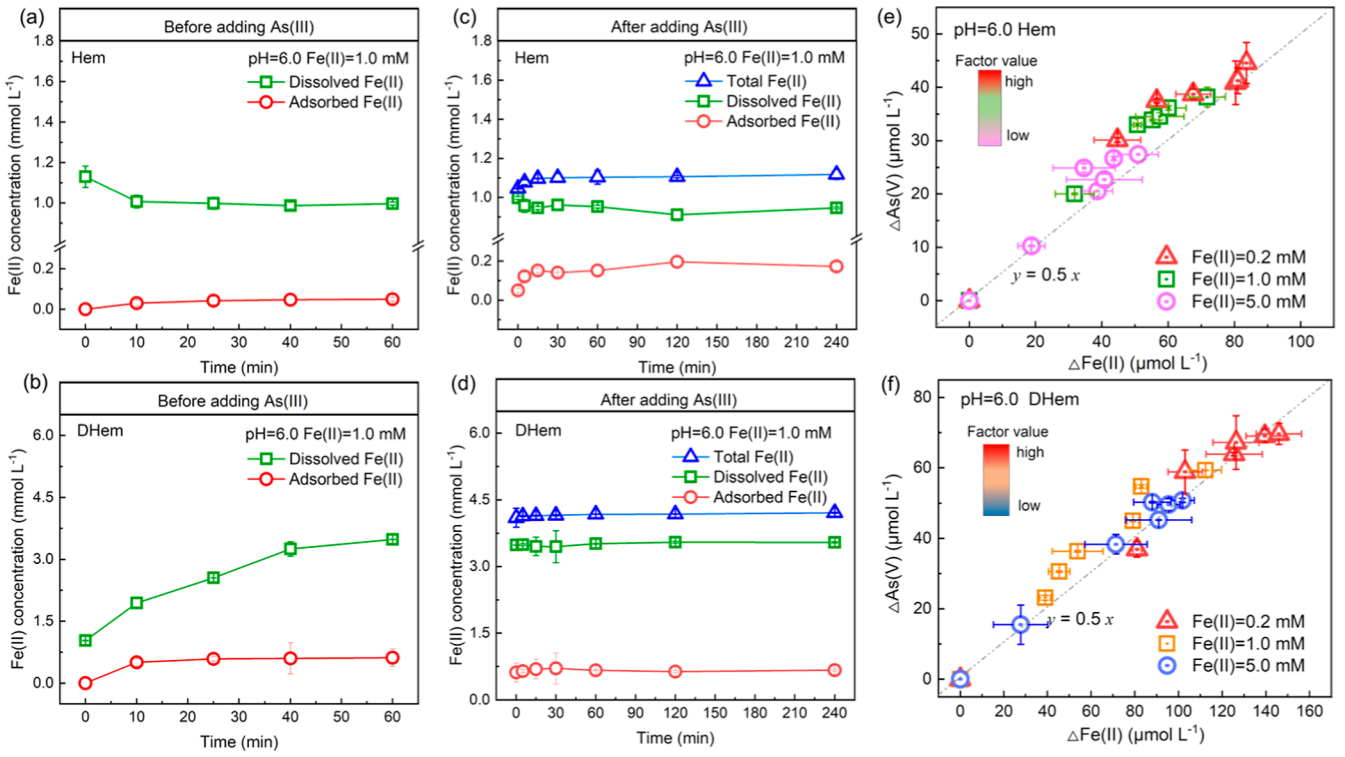

Figure 2. Fe(II) concentration on the surface of Hem and DHem (1.0 g L^{-1}) under anoxic conditions. The temporal evolution of Fe(II) concentration (1.0 mM) before (a,b) and after adding As(III) (c,d). The relationship of As(V) yield with the amount of oxidized Fe(II) under varying conditions on Hem (e) and DHem samples (f).

of structural Fe(III), which limit efficient interfacial electron transfer. The residual As(III) concentration in solution for the DHem system was lower than that for the Hem system after the reaction reached equilibration. This result suggested that DHem has a higher adsorption capacity for As species compared to Hem, which was attributed to the stronger adsorption affinity of oxygen vacancy sites in DHem to arsenic species.[12,21,22] In contrast to the mineral alone system, the As(III) concentration in mineral suspensions sharply decreased within the initial 10 min after addition of 1.0 mM Fe(II) (Figure 1c,d). We observed a fast generation of As(V) species in the hematite−Fe(II) system within the initial 30 min, indicating that the presence of Fe(II) is beneficial for As(III) oxidation. The specific surface areas (SSA) for Hem and DHem samples were 21.3 and 25.3 m^2/g, respectively. To account for the influence of SSA on As(III) oxidation over hematite samples, the formed As(V) concentrations were normalized by their SSA values (Figure 1e). This calculation revealed that the formed As(V) concentration amount per unit surface area was higher for the DHem sample compared to Hem at Fe(II) concentrations from 0 to 5.0 mM. Remarkably, the formed As(V) concentration at 240 min in the DHem−Fe(II) system (about 59.4 μmol L^{-1}) was considerably higher than that in the Hem−Fe(II) system (38.1 μmol L^{-1}) at the 1.0 mM Fe(II) concentration (Figures 1e,f, and S3). We also examined the effect of solution pH on the anoxic As(III) oxidation in the mineral-Fe(II) system with 1.0 mM Fe(II). Compared to pH 7, the relatively lower pH (e.g., pH 5) was favorable to the anoxic As(III) oxidation in the hematite−Fe(II) systems (Figure S4). Interestingly, although the concentrations of As(V) formed in the hematite−Fe(II) setups at varying initial Fe(II) and solution pH differed significantly, the total As(V) concentration formed in the DHem−Fe(II) system was always higher than that in the Hem−Fe(II) system. This result indicated that the presence of vacancy defects in hematite favorably facilitated anoxic As(III) oxidation in hematite−Fe(II) systems.

To illustrate the evolution of Fe(II) species in the Hem− and DHem−Fe(II) couples, we quantified the concentrations of dissolved and adsorbed Fe(II) as a function of time. Before adding As(III), the dissolved Fe(II) concentration in Hem−Fe(II) systems decreased and stabilized within 30 min, while the adsorbed Fe(II) concentration gradually increased (Figures 2a and S5). This indicates that Fe(II) adsorption occurs on the Hem surface. Compared to the Hem−Fe(II) system, a notable increase in the dissolved Fe(II) concentration (3.2 mM) after 60 min was observed in the DHem−Fe(II) system, which was significantly higher than the initially added Fe(II) concentration of 1.0 mM (Figure 2b). The occurrence of partial reductive dissolution of structural Fe(III) to Fe(II) species on the DHem sample implies a significant difference in Fe(II) solution chemistry behavior compared to experiments with Hem. After addition of As(III) to the Hem−Fe(II) setups, the total Fe(II) concentration showed a slight increase (1.10 mM) after the reaction reached equilibrium (Figure 2c), while we observed a stronger increase in the DHem−Fe(II) setups (4.21 mM) (Figure 2d).

We compared the extent of Fe(II) concentration increase with the As(V) yield under different Fe(II) addition conditions. As shown in Figure 2e,f, there was an excellent linear relationship between the increase of As(III) oxidation (Δ[As(V)]) and Fe(II) concentration (Δ[Fe(II)]). According to previous reports, As(III) oxidation in Fe(III) oxide−Fe(II) systems is a two-electron transfer process,[23] where surface-bound As(III) donates electrons to the structural Fe(III) of hematite samples.[24] In our study, we observed that the slopes

https://doi.org/10.1021/acs.langmuir.6c02392
Langmuir 2026, 42, 19343−19353

Downloaded from pubs.acs.org/langd5/article-pdf/42/26/19343/6521356l/acs.langmuir.6c02392.pdf by UNIV TUEBINGEN user on 17 September 2026

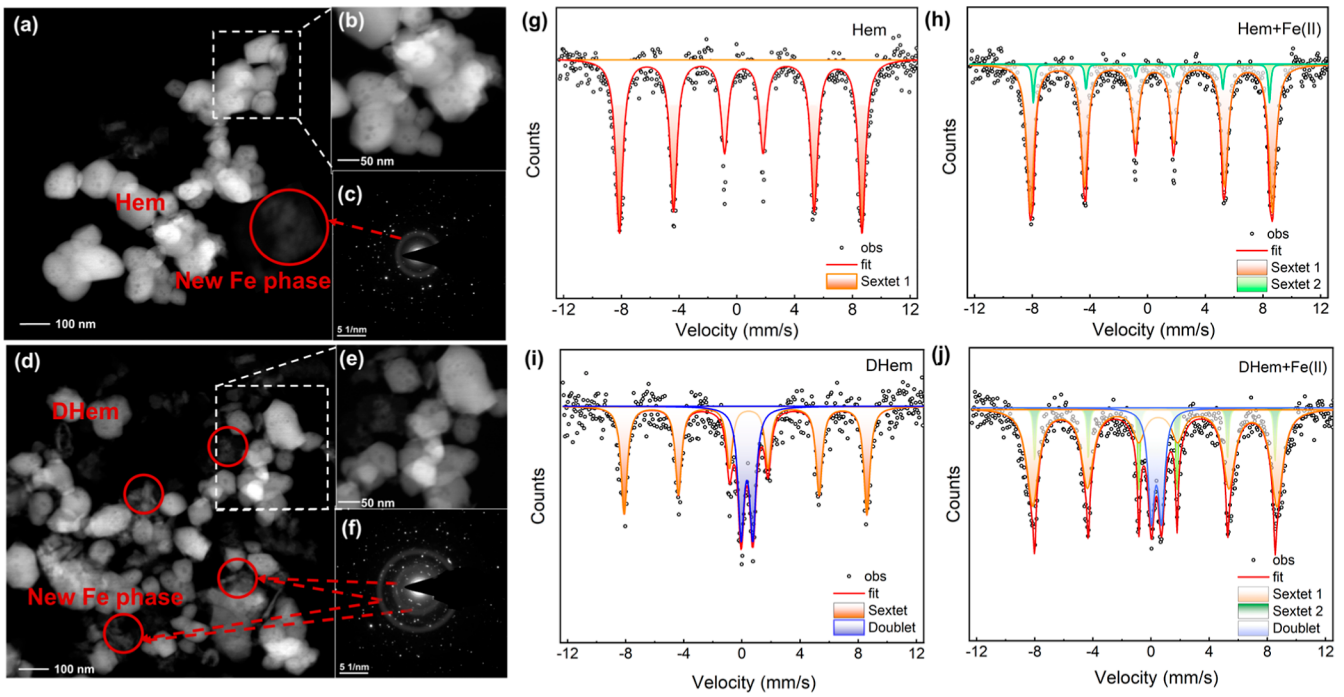

Figure 3. TEM mapping-SAED of Hem (a–c) and DHem (d–f) after the reaction with Fe(II) (1.0 mM) for 1 h. Mössbauer spectra of Hem and DHem samples with (g,h) and without (i,j) addition of 1.0 mM Fe(II) at pH 6.0. The Mössbauer spectra were collected at 273 K.

of Δ[As(V)]/Δ[Fe(II)] in our hematite–Fe(II) couples were close to 0.5, indicating a good electron balance between As(V) generation and Fe(III) reduction. This result revealed that anoxic As(III) oxidation by hematite–Fe(II) couples is a nonradical process, and no other abiotic factors, such as reactive oxygen species (ROS), are involved in As(III) oxidation.[24,25]

3.2. Formation of Active Metastable Iron Phases in the Hematite–Fe(II) System

Based on our results, the question arises why the presence of oxygen vacancies promotes As(III) oxidation in hematite–Fe(II) systems. Theoretically, the strong As(III) oxidation ability of hematite–Fe(II) should be attributed to the availability of electron acceptors, such as structural Fe(III) species in the hematite. However, we did not observe As(III) oxidation on hematite alone, indicating the role of other electron acceptors contributing to the As(III) oxidation. Previous reports have observed that poorly crystalline iron minerals (e.g., ferrihydrite and hydrated Fe(III) oxide) represent active metastable iron phases, which could trigger As(III) oxidation in both oxic and anoxic environments.[26,27] To explore whether the higher As(III) oxidation observed in DHem–Fe(II) systems compared to Hem–Fe(II) systems originates from the formation of more reactive metastable iron(III) phases, the evolution of mineral phases was examined using HRTEM combined with SAED mapping. The HRTEM images revealed a cubic-like morphology commonly found in hematite with exposed (012) facets (Figure S1). After adding Fe(II), newly formed iron minerals appeared (denoted in red circles) (Figure 3a,b,d,e). These newly formed iron minerals exhibited relatively poor crystallinity with flocculent and irregular morphologies, as evidenced by our HRTEM analysis (Figure 3c,f) similar to previous work reported by Jeon et al.[28] XRD patterns revealed that Fe(II)-reacted hematite still contained mainly hematite as the crystalline mineral phase (Figure S6), suggesting that no significant phase transformation occurred after Fe(II) addition. This phenomenon was also observed in previous work, which was attributed to the oxidative adsorption of Fe(II) to structural Fe(III) in the hematite lattice to form new hematite phases.[28−31] However, the intensity of the diffraction signals in Fe(II)-reacted hematite became smaller, indicating that the structure of the newly formed hematite was obviously different from that of the pristine hematite. Catalano et al. employed X-ray reflectivity measurements to confirm that Fe(II) induces changes of the hematite structure,[29] showing nanoscale size, high structural relaxation, and pronounced defect features. They also proposed that Fe(II)-induced structural transformation in hematite enables the newly formed iron phases to exhibit high reactivity toward redox-sensitive contaminants. Therefore, the newly formed active hematite minerals in our study were likely analogous to the active metastable iron phases generated during the oxidative adsorption of Fe(II) on iron oxyhydroxide minerals.[32,33] Interestingly, HRTEM images showed distinct morphological features of newly formed active iron minerals in the DHem–Fe(II) system compared to the Hem–Fe(II) system (Figure 3a,e).

To further confirm the higher content of active metastable iron phases in DHem–Fe(II) sample compared to Hem–Fe(II) sample, we employed Mössbauer spectroscopy to analyze the evolution of iron mineral phases in Hem and DHem samples before and after Fe(II) addition at pH 6. As shown in Figure 3g, the Hem sample (no Fe(II) addition) was characterized by a typical magnetic splitting spectrum with a single sextet.[30] The single sextet featured a center shift (CS) of ~0.37 mm s^{-1}, a quadrupole splitting (QS) of ~−0.22 mm s^{-1}, and a magnetic hyperfine field (H) of ~52.3 T (Table S3), which are typical parameters for hematite.[34] For DHem (no Fe(II) addition), except for a typical sextet, a new doublet was also observed in the Mössbauer profile (Figure 3i). The doublet showed a CS of ~0.35 mm s^{-1} and a QS of 0.8 mm s^{-1}

https://doi.org/10.1021/acs.langmuir.6c02392
Langmuir 2026, 42, 19343−19353

Downloaded from pubs.acs.org/langd5/article-pdf/42/26/19343/6521356l/acs.langmuir.6c02392.pdf by UNIV TUEBINGEN user on 17 September 2026

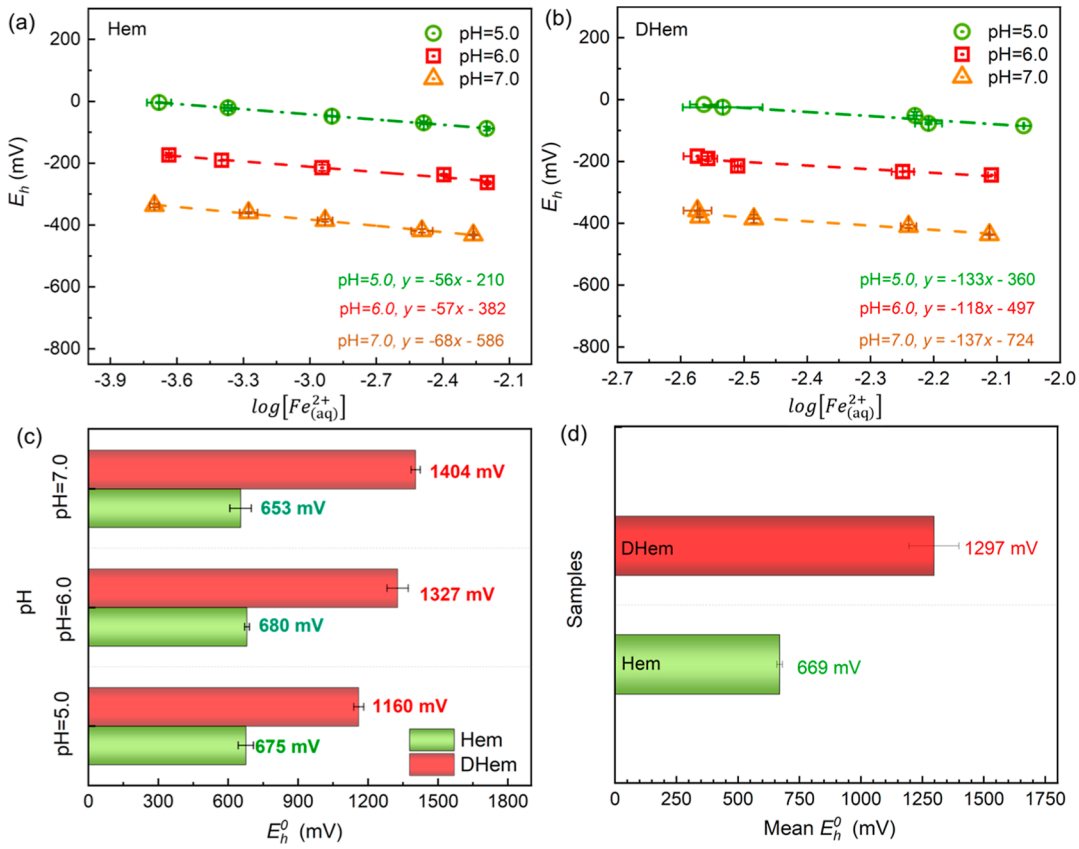

Figure 4. E_H values of Hem (a) and DHem (b) suspensions as a function of $\log[Fe^{2+}_{(aq)}]$ at pH 5.0, 6.0, and 7.0; calculated E^0_H values of minerals at different pH (c) and their corresponding average E^0_H values (d). Experiment condition: 25 mM KCl, 0.2−5.0 mM Fe(II), 20 μM mediator, 1 g L^{-1} mineral suspensions, and 24 h equilibrium time.

that can be assigned to a new Fe atomic environment in the DHem structure formed by the partial transition of Fe(III) to Fe(II) due to the presence of oxygen vacancies.[12,21] After adding Fe(II) to the minerals, in addition to the typical hematite sextet (sextet 1 in orange), the Mössbauer spectra of Fe(II)-reacted Hem and DHem samples showed an additional sextet (sextet 2 in green) with similar Mössbauer fitting parameters as sextet 1 but with a relatively low H value (Figure 3h,j). The change of H in sextet 2 was probably due to the fact that the Fe(II)-catalyzed transformation altered the magnetic properties of Fe(II)-reacted hematite compared to bulk hematite.[30,35] This phenomenon was also observed in the Fe(II)−goethite redox system.[36] Notably, the relative fraction of this reactive iron mineral component formed in the DHem−Fe(II) couple was 12.3%, which was significantly higher than that formed in the Hem−Fe(II) couple (7.0%). This result indicated that the presence of oxygen vacancies in hematite facilitates the formation of active metastable iron phases after addition of Fe(II) to hematite.

3.3. Thermodynamic Insights into the Formation of Active Iron Phases Promoted by Oxygen Vacancies

While we observed a higher content of the reactive iron(III) phase in the DHem−Fe(II) system, the underlying mechanism of how oxygen vacancies facilitated the formation of this reactive iron phase is still unclear. In general, the formation of active metastable iron phases involves electron transfer (ET) between sorbed Fe(II) and the bulk hematite surface. The higher the oxidative potential of the bulk hematite is, the more thermodynamically favorable the ET between surface-bound Fe(II) and the mineral is. In this study, we utilized an optimized mediated potentiometry method[6,14,37] to determine the standard reduction potential (E^0_H) of hematite for further illustrating the effect of oxygen vacancies on the ET. The half-reaction that contains hematite (α-Fe_2O_3(s)) and aqueous Fe^{2+} ($Fe^{2+}_{(aq)}$) is described below.

$$\frac{1}{2}\alpha\text{-}Fe_2O_3(s) + 3H^+ + e^- = Fe^{2+}_{(aq)} + \frac{3}{2}H_2O \quad (1)$$

The Nernst equation corresponding to the above half-reaction is as follows

$$E_H = E^0_H - \frac{RT}{F}\ln[Fe^{2+}_{(aq)}] + 3\frac{RT}{F}\ln[H^+] \quad (2)$$

where E_H and E^0_H are the reduction potential and standard reduction potential of hematite suspensions, respectively, $Fe^{2+}_{(aq)}$is the equilibrium concentration of aqueous Fe^{2+} in a binary heterogeneous system, $[H^+]$ is the concentration of H^+ in solution, R is the ideal gas constant, T is the temperature (K), and F is the Faraday constant. At room temperature (298 K), eq 2 is simplified as follows

$$E_H = E^0_H - 0.059V\cdot\log[Fe^{2+}_{(aq)}] - 0.177\ V\cdot pH \quad (3)$$

For DHem, its structural formula can be expressed as α-Fe_2O_{3-x}, where x represents the stoichiometric number of oxygen vacancies in the DHem. The corresponding half-reaction and Nernst equation for the DHem are as follows

https://doi.org/10.1021/acs.langmuir.6c02392
Langmuir 2026, 42, 19343−19353

Downloaded from pubs.acs.org/langd5/article-pdf/42/26/19343/6521356l/acs.langmuir.6c02392.pdf by UNIV TUEBINGEN user on 17 September 2026

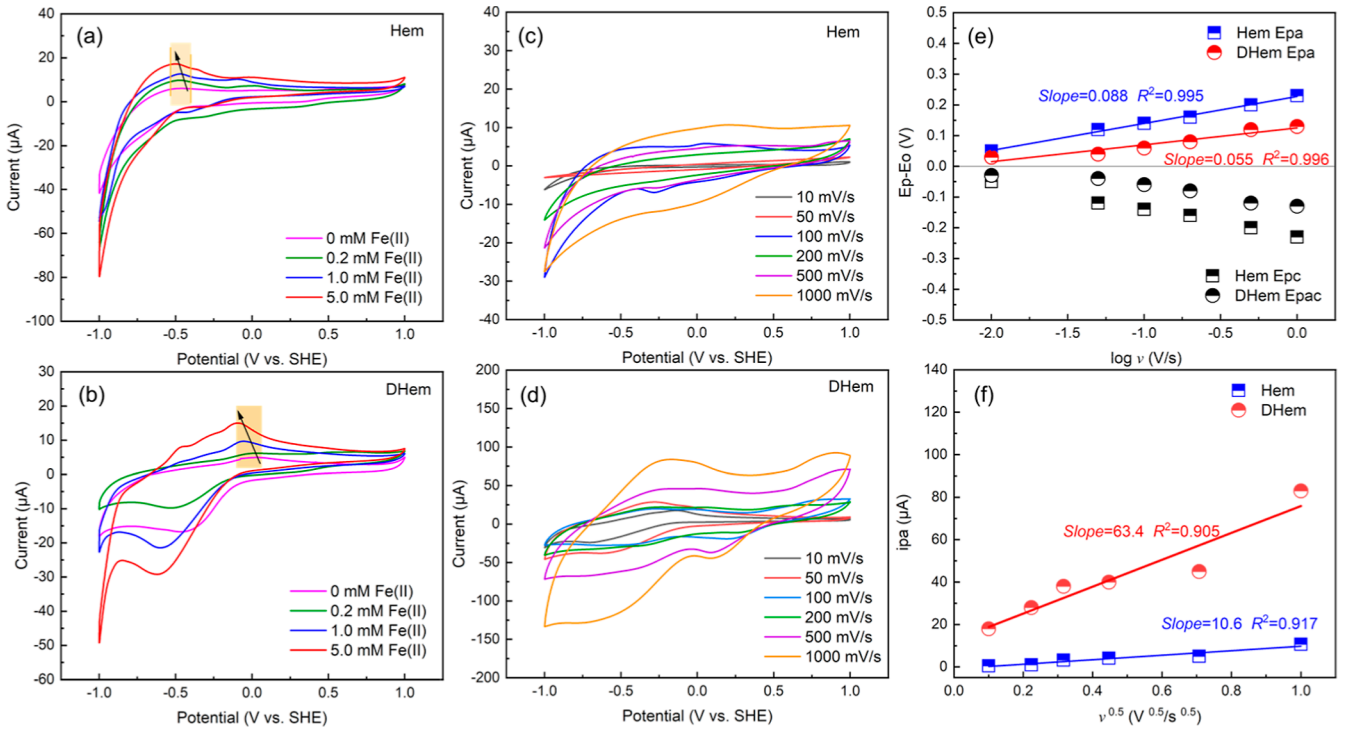

Figure 5. CV curves of the Fe(II) reaction on Hem (a) and DHem (b) at pH = 6.0; the CV curves of the Fe(II) (1.0 mM) reaction on Hem (c) and DHem (d) samples at different scan rates (0.01−1 mV s^{-1}); the anodic peak potentials (E_{pa}) *vs* logν (e), and the corresponding anode peak current (i_{pa}) *vs* $\nu^{0.5}$ (f) of the CV curves mentioned above using electrode coating with Hem or DHem powders.

$$\frac{1}{2}\alpha\text{-}Fe_2O_{3-x}(s) + (3-x)H^+ + (1-x)e^- = Fe^{2+}_{(aq)} + \frac{3-x}{2}H_2O \quad (4)$$

$$E_H = E^0_H - \frac{RT}{(1-x)F}\ln[Fe^{2+}_{(aq)}] + (3-x)\frac{RT}{(1-x)F}\ln[H^+] \quad (5)$$

We have measured the x value, that is, 0.518 (see Section 2.1). At room temperature, we simplified eq 5 by substituting the value of x into the equation.

$$E_H = E^0_H - 0.122\ V\cdot\log[Fe^{2+}_{(aq)}] - 0.304V\cdot pH \quad (6)$$

Figure 4 illustrates the evolution of the E_H value as a function of $\log[Fe^{2+}_{(aq)}]$ at pH 5.0, 6.0, and 7.0. As shown in Figure 4a,b, the relationship between $\log[Fe^{2+}_{(aq)}]$ and E_H could be well fitted by a linear regression equation at a given pH. For the Hem sample, the slopes obtained from the linear regression equation at pH 5.0, 6.0, and 7.0 were −0.056 V, −0.057 V, and −0.068 V, respectively, which were very close to the theoretical Nernstian slope value shown in eq 3 (−0.059 V). The slopes for the DHem sample at pH 5.0 (−0.133 V), 6.0 (−0.118 V), and 7.0 (−0.137 V) were also very close to the theoretical values (−0.122 V) shown in eq 6, suggesting that the Nernst equation could better describe the evolution of E_H in the Fe(II)−hematite couples. This result also demonstrates that under relatively low Fe(II) concentration (0.02 mM) and low pH (5.0) conditions, the system exhibits a higher E_H, which can also be theoretically inferred from eqs 3 and 6. The resulting increase in E_H thermodynamically favors enhanced oxidizing power and prolonged persistence of reactive Fe(III) species, which provides a mechanistic explanation for the higher As(III) oxidation efficiency observed under acidic conditions (Figure 1e).

As the y-intercept in the linear regression equation corresponds to the E^0_H value in eqs 2 and 6, we therefore further calculated the E^0_H of hematite samples at different pH values using the corresponding regression equations. The calculated E^0_H values of hematite samples at given pH values were very close to each other (Figure 4c), indicating that the mediated potentiometric method used for standard reduction potential calculation was highly reliable. Remarkably, the calculated average E^0_H of DHem was +1.297 V, which was nearly two times larger than that of Hem (+0.669 V) (Figure 4d). The relatively larger E^0_H of DHem compared to that of Hem suggests a strong electron-transfer interaction with surface-bound Fe(II), thereby thermodynamically favoring the formation of the active metastable iron phases involved in As(III) oxidation.

3.4. Electrochemical Evidence of Enhanced Electron Transfer between Fe(II) and Defective Hematite

To comparatively evaluate the interfacial electron-transfer behavior of Fe(II) on the Hem and DHem surfaces, cyclic voltammetry (CV) measurements were performed. As shown in Figure 5a,b, the mineral suspensions without Fe(II) addition showed very weak redox currents, indicating that the hematite alone has very low intrinsic electrochemical activity. This explains why we did not observe As(III) oxidation by hematite alone (Figure 1a,b). Interestingly, the intensity of the redox current peak gradually increased with increasing Fe(II) concentration in the mineral suspensions. In addition to the increased intensity of the redox peak, we also observed a shift of the peak position (shaded region) after addition of Fe(II). Apparently, the potential of the oxidation peak in the DHem−

https://doi.org/10.1021/acs.langmuir.6c02392
Langmuir 2026, 42, 19343−19353

Downloaded from pubs.acs.org/langd5/article-pdf/42/26/19343/6521356l/acs.langmuir.6c02392.pdf by UNIV TUEBINGEN user on 17 September 2026

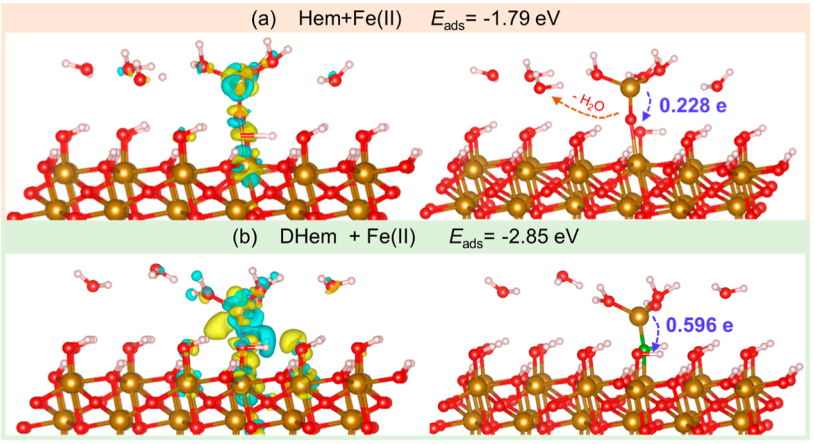

Figure 6. Optimized structure of the Fe(II) reaction on the surface of hematite in the absence (a) and presence of one oxygen vacancy (b). The brown, red, and white spheres represent Fe, O, and H atoms, respectively. The adsorbed hydrated Fe(II) molecules used in this study are $Fe(OH)(OH_2)_3$. Yellow and cyan iso surfaces represent charge accumulation and depletion, respectively.

Fe(II) couple (Fe(II) = 5.0 mM) was −0.107 V, which was less negative than that in the Hem−Fe(II) couple (−0.508 V), suggesting that the DHem−Fe(II) couple exhibited a stronger ET ability than the Hem−Fe(II) couple.

To further quantify the rate constants (k_s) of electron transfer in hematite−Fe(II) couples, we recorded CV curves of the Fe(II) reaction on hematite samples at different scan rates ranging from 0.1 to 1.0 V s^{-1} (Figure 5c,d) to plot the linear relationship between $E_p - E_0$ and the log of the scan rate (log$v$) (Figure 5e) based on the Laviron equation.[38−40]

$$E_P - E_0 = -\frac{2.303RT}{\alpha nF}\log v - \frac{2.303RT}{\alpha nF}\log\frac{\alpha nF}{RTk_s} \quad (8)$$

where α is the charge transfer coefficient, n is the number of electrons transferred (n = 1 in this study), v is the scan rate, E_0 is the apparent formal redox potential estimated by the average between anodic peak potential ($E_{p,a}$) and cathodic peak potential ($E_{p,c}$), k_s is the apparent rate constant of electron transfer between the oxides and Fe(II), and R, T, and F are the universal gas constant (8.314 J mol^{-1} K^{-1}), absolute temperature (298 K), and Faraday constant (96485 C), respectively. According to eq 8, the value of k_s can be obtained from eq 8 when $E_p - E_0 = 0$ ($k_s = \frac{\alpha Fv}{RT}$). The calculated slope for the Fe(II) reaction on Hem was 0.088 s^{-1}, which was 1.6 times larger than that on DHem (0.055 s^{-1}). A larger absolute slope in the $E_p - E_0$ versus log$v$ relationship corresponds to a smaller charge transfer coefficient (α), suggesting increased irreversibility of the electron-transfer process. As described by $k_s = \frac{\alpha Fv}{RT}$, a smaller α under identical scan-rate conditions necessarily leads to a lower apparent rate constant (k_s). Accordingly, the relatively larger slope observed for Hem corresponds to a smaller k_s, indicating more kinetically constrained interfacial electron transfer on Hem compared to DHem. In addition to k_s, the diffusion coefficient of the charge carrier, which could be used to reflect the reaction rate between the oxide and Fe(II), was also calculated based on Randles−Sevcik equation.[41−43]

$$I_p = 0.4463\,(nF)^{3/2}AC\left(\frac{D_O}{RT}\right)^{1/2}v^{1/2} \quad (9)$$

where I_p is the peak current (μA) at scan rate v, n is the number of electrons involved in the reaction, and A and C are the area of the electrode and the concentration of the redox active molecule in the reaction, respectively. D_0 is the diffusion coefficient of a charge carrier. We plotted the anodic peak current (I_{pa}) against the square root of the scan rate ($v^{1/2}$), which showed a good straight line (Figure 5e). As the area of the electrode and the initial Fe(II) concentration used in our electrochemical experiments are the same, the slope of the fitted straight line therefore directly reflects the diffusion coefficient. As shown in Figure 5f, the fitted slope for DHem−Fe(II) couples was 63.4, which was far larger than that of Hem−Fe(II) couple (10.6), indicating that $Fe^{2+}_{(aq)}$could rapidly move to the DHem surface. This result revealed that oxygen vacancies in hematite not only facilitated the electron transfer between Fe(II) and the mineral but also accelerated the diffusion of $Fe^{2+}_{(aq)}$ to the mineral surface, thereby boosting the formation of active metastable iron phases.

3.5. Chemical Bonding Analysis of Fe(II) on Hematite in the Presence of Oxygen Vacancies

To further reveal the effect of oxygen vacancies on electron transfer in iron oxide−Fe(II) couples, DFT calculations, a useful tool to observe the interfacial behavior of Fe(II) on hematite directly, were employed to analyze the chemical bonding of Fe(II) on hematite both in the absence and presence of oxygen vacancies. Figure 6 shows the constructed model of Fe(II) adsorbed on both pristine hematite and hematite with one oxygen vacancy. For the pristine hematite surface, the calculated adsorption energy (E_{ads}) of Fe(II) on the mineral surface was −1.79 eV. When Fe(II) adsorbed on the oxygen vacancy site of the defective hematite surface, its E_{ads} significantly decreased from −1.79 to −2.85 eV, indicating that Fe(II) adsorption on the surface of defective hematite is more thermodynamically favorable. This phenomenon was also observed in our previous work using arsenic species as a probe molecule; i.e., the surface oxygen vacancy of hematite is the active site for ion adsorption.[12,21,44] To illustrate the effect of oxygen vacancies on the electronic density distributions of Fe(II) bound to the mineral, the charge density difference of Fe−O binding was analyzed. The charge density difference analysis revealed a distinct depletion of localized electrons for the surface-bound Fe(II) (cyan isosurface), while the oxygen site of minerals bound to Fe(II) species showed an

https://doi.org/10.1021/acs.langmuir.6c02392
Langmuir 2026, 42, 19343−19353

Downloaded from pubs.acs.org/langd5/article-pdf/42/26/19343/6521356l/acs.langmuir.6c02392.pdf by UNIV TUEBINGEN user on 17 September 2026

accumulation of electrons (yellow isosurface) (Figure 6). However, the extent of net electron transfer in the defective hematite was different from that in the defect-free hematite; i.e., approximately 0.228*e* Bader charges were observed to transfer from adsorbed Fe(II) to the hematite bulk, which was lower than that observed in the hematite bulk with one oxygen vacancy (0.596*e*) (Table S4). This observation suggested that the oxygen vacancies on hematite act as stronger electron acceptors, facilitating a greater transfer of charge from the Fe(II) atoms to the lattice, in agreement with our electrochemical evidence (Figure 5). Overall, our electrochemical and DFT calculations provide experimental and theoretical evidence to reveal that the oxygen vacancy defects play a critical role in improving the oxidation potential of hematite, which favors the formation of the newly active metastable iron phases for the following As(III) oxidation.

4. CONCLUSIONS

In summary, we systematically analyzed the structural evolution of Fe(III) minerals following reductive Fe(II) release and identified oxygen vacancy defects as intrinsic features of natural Fe(III) minerals. We demonstrated that oxygen vacancies in hematite promoted the formation of new reactive Fe phases, thereby enhancing As(III) oxidation in hematite−Fe(II) systems across a range of pH values and Fe(II) concentrations. Thermodynamic and kinetic analyses further revealed that defective hematite exhibits a higher standard redox potential than defect-free hematite, favoring electron transfer and diffusion processes that drive the generation of reactive Fe(III) intermediates. Complementary DFT calculations confirmed that oxygen vacancy sites on hematite surfaces act as stronger electron acceptors, facilitating the charge transfer from Fe(II) to the mineral lattice. This study highlights that the microstructure evolution of Fe(III) minerals after reductive release of Fe(II) to form oxygen vacancies is an important, but so far overlooked, factor that drives the generation of more active Fe(III) phases. Given the strong dependence of arsenic mobility and toxicity on its oxidation state, this study not only provides new thermodynamic insights into anoxic As(III) oxidation in mineral-Fe(II) systems but also advances our understanding of arsenic fate and transport in iron-rich anoxic environments.

■ ASSOCIATED CONTENT

Supporting Information

The Supporting Information is available free of charge at https://pubs.acs.org/doi/10.1021/acs.langmuir.6c02392.

Details of characterization for XRD, SEM, TEM, EPR, and TG−MS; Fe(II) and As(III) oxidation process on the surface of Hem and DHem samples under anoxic conditions; fitted Mössbauer spectra of Hem and DHem samples at 273 K before and after reaction with Fe(II); and additional figures and tables (PDF)

■ AUTHOR INFORMATION

Corresponding Author

Jingtao Hou − *State Environmental Protection Key Laboratory of Soil Health and Green Remediation, Hubei Key Laboratory of Soil Environment and Pollution Remediation, College of Resources and Environment, Huazhong Agricultural University, Wuhan 430070, China;* orcid.org/0000-0002-2472-8309; Email: jthou@mail.hzau.edu.cn, houjt87@163.com

Authors

Juan Liu − *State Environmental Protection Key Laboratory of Soil Health and Green Remediation, Hubei Key Laboratory of Soil Environment and Pollution Remediation, College of Resources and Environment, Huazhong Agricultural University, Wuhan 430070, China*

Siyuan Zheng − *State Environmental Protection Key Laboratory of Soil Health and Green Remediation, Hubei Key Laboratory of Soil Environment and Pollution Remediation, College of Resources and Environment, Huazhong Agricultural University, Wuhan 430070, China*

Juan Xiong − *State Environmental Protection Key Laboratory of Soil Health and Green Remediation, Hubei Key Laboratory of Soil Environment and Pollution Remediation, College of Resources and Environment, Huazhong Agricultural University, Wuhan 430070, China;* orcid.org/0000-0003-4414-536X

Mingxia Wang − *State Environmental Protection Key Laboratory of Soil Health and Green Remediation, Hubei Key Laboratory of Soil Environment and Pollution Remediation, College of Resources and Environment, Huazhong Agricultural University, Wuhan 430070, China;* orcid.org/0000-0002-5244-432X

Andreas Kappler − *Geomicrobiology, Department of Geosciences, University of Tübingen, Tübingen 72076, Germany;* orcid.org/0000-0002-3558-9500

Wenfeng Tan − *State Environmental Protection Key Laboratory of Soil Health and Green Remediation, Hubei Key Laboratory of Soil Environment and Pollution Remediation, College of Resources and Environment, Huazhong Agricultural University, Wuhan 430070, China*

Complete contact information is available at: https://pubs.acs.org/10.1021/acs.langmuir.6c02392

Notes

The authors declare no competing financial interest.

■ ACKNOWLEDGMENTS

This work was supported by the National Natural Science Foundation of China (42277015, 42277302, 41977022), the Major Science and Technology Project of Hubei Province (2023BBA003), Hubei Provincial Natural Science Foundation (2026AFC0644), Innovative Research Group Project of Hubei Provincial Natural Science Foundation (2023AFA009), and the Fundamental Research Funds for the Central Universities (2662025ZHPY005). We thank Prof. Yuanzhi Li at Wuhan University of Technology for his help with DFT calculations.

■ REFERENCES

(1) Podgorski, J.; Berg, M. Global Threat of Arsenic in Groundwater. *Science* **2020**, *368* (6493), 845−850.

(2) Chen, G.; Shi, H.; Tao, J.; Chen, L.; Liu, Y.; Lei, G.; Liu, X.; Smol, J. P. Industrial Arsenic Contamination Causes Catastrophic Changes in Freshwater Ecosystems. *Sci. Rep.* **2015**, *5* (1), 17419.

(3) Wang, J.; Liu, J.; Peng, X.; He, M.; Hu, X.; Zhao, J.; Zhu, F.; Yang, X.; Kong, L. Reductive Removal of As(V) and As(III) from Aqueous Solution by the UV/Sulfite Process: Recovery of Elemental Arsenic. *Water Res.* **2022**, *223*, 118981.

(4) Li, X.; Guo, C.; Pillai, S. C.; Jin, X.; Yao, Q.; Bao, Y.; Jiang, X.; Lu, G.; Wang, H.; Dang, Z. Facet-Dependent Competitive Adsorption

Downloaded from pubs.acs.org/langd5/article-pdf/42/26/19343/6521356l/acs.langmuir.6c02392.pdf by UNIV TUEBINGEN user on 17 September 2026

Mechanisms of Chromate and Oxalic Acid on γ-FeO(OH) Nanocrystals. *Langmuir* **2023**, *39* (41), 14539−14549.
(5) Cheng, W.; Marsac, R.; Hanna, K.; Boily, J. F. Competitive Carboxylate-Silicate Binding at Iron Oxyhydroxide Surfaces. *Langmuir* **2021**, *37* (44), 13107−13115.
(6) Stewart, S. M.; Hofstetter, T. B.; Joshi, P.; Gorski, C. A. Linking Thermodynamics to Pollutant Reduction Kinetics by Fe(II) Bound to Iron Oxides. *Environ. Sci. Technol.* **2018**, *52* (10), 5600−5609.
(7) Li, X.; Liu, L.; Wu, Y.; Liu, T. Determination of the Redox Potentials of Solution and Solid Surface of Fe(II) Associated with Iron Oxyhydroxides. *ACS Earth Space Chem.* **2019**, *3* (5), 711−717.
(8) Perez, J. P. H.; Tobler, D. J.; Thomas, A. N.; Freeman, H. M.; Dideriksen, K.; Radnik, J.; Benning, L. G. Adsorption and Reduction of Arsenate during the Fe(II)-Induced Transformation of Ferrihydrite. *ACS Earth Space Chem.* **2019**, *3* (6), 884−894.
(9) Amstaetter, K.; Borch, T.; Larese-Casanova, P.; Kappler, A. Redox Transformation of Arsenic by Fe(II)-Activated Goethite (α-FeOOH). *Environ. Sci. Technol.* **2010**, *44*, 102−108.
(10) Notini, L.; Latta, D. E.; Neumann, A.; Pearce, C. I.; Sassi, M.; N'Diaye, A. T.; Rosso, K. M.; Scherer, M. M. The Role of Defects in Fe(II)-Goethite Electron Transfer. *Environ. Sci. Technol.* **2018**, *52* (5), 2751−2759.
(11) Fang, L.; Hong, Z.; Borch, T.; Shi, Q.; Li, F. Iron Vacancy Accelerates Fe(II)-Induced Anoxic As(III) Oxidation Coupled to Iron Reduction. *Environ. Sci. Technol.* **2023**, *57* (5), 2175−2185.
(12) Liu, J.; Xiang, Y.; Chen, Y.; Zhang, H.; Ye, B.; Ren, L.; Tan, W.; Kappler, A.; Hou, J. Quantitative Contribution of Oxygen Vacancy Defects to Arsenate Immobilization on Hematite. *Environ. Sci. Technol.* **2023**, *57* (33), 12453−12464.
(13) Tamura, H.; Goto, K.; Yotsuyanagi, T.; Nagayama, M. Spectrophotometric Determination of Iron(II) with 1,10-Phenanthroline in the Presence of Large Amounts of Iron(III). *Talanta* **1974**, *21* (4), 314−318.
(14) Chen, G.; Thompson, A.; Gorski, C. A. Disentangling the Size-Dependent Redox Reactivity of Iron Oxides Using Thermodynamic Relationships. *Proc. Natl. Acad. Sci. U. S. A* **2022**, *119* (40), No. e2204673119.
(15) Gorski, C. A.; Edwards, R.; Sander, M.; Hofstetter, T. B.; Stewart, S. M. Thermodynamic Characterization of Iron Oxide−Aqueous Fe(II) Redox Couples. *Environ. Sci. Technol.* **2016**, *50* (16), 8538−8547.
(16) Yan, L.; Chan, T.; Jing, C. Mechanistic Study for Antimony Adsorption and Precipitation on Hematite Facets. *Environ. Sci. Technol.* **2022**, *56* (5), 3138−3146.
(17) Zheng, C.; Zhong, W.; Yan, L.; Jing, C. Facet-Dependent Atomic Distances Shape Vanadate Adsorption Complexes on Hematite Nanocrystals. *Langmuir* **2023**, *39* (3), 949−956.
(18) Tang, X.; Chen, J.; Chen, Y. A Density Functional Based Tight Binding (DFTB+) Study on the Sulfidization-Xanthate Flotation Mechanism of Cerussite. *Appl. Surf. Sci.* **2023**, *612*, 155677.
(19) Yan, L.; Chan, T.; Jing, C. Arsenic Adsorption on Hematite Facets: Spectroscopy and DFT Study. *Environ. Sci.:Nano* **2020**, *7* (12), 3927−3939.
(20) Hong, Z.; Li, F.; Borch, T.; Shi, Q.; Fang, L. Incorporation of Cu into Goethite Stimulates Oxygen Activation by Surface-Bound Fe(II) for Enhanced As(III) Oxidative Transformation. *Environ. Sci. Technol.* **2023**, *57* (5), 2162−2174.
(21) Liu, J.; Hou, J.; Xiong, J.; Ren, L.; Wang, M.; Tan, W.; Kappler, A. Quantitative Enhancement of Arsenate Immobilization Induced by Vacancy Defects on Various Exposed Lattice Facets of Hematite. *Environ. Sci. Technol.* **2025**, *59* (5), 2802−2814.
(22) Xiang, Y.; Hou, J.; Ren, L.; Xiong, J.; Wan, B.; Wang, M.; Tan, W.; Kappler, A. Spontaneous Abiotic Reduction of Arsenate to Arsenite Mediated by Structural Fe(II) Resulting from Oxygen Vacancy Clusters in Ferrihydrite. *Environ. Sci. Technol.* **2025**, *59* (10), 5191−5201.
(23) Li, X.; Hai, G.; Chen, G.; Liu, J.; Zhao, F.; Zhou, J.; Leung, M. K. H.; Wang, H. Unique Two-Electron Transfer Pathway of Bismuth Nanocrystal for Enhanced N_2 Electroreduction Revealed by in Situ Infrared Spectroscopy. *Appl. Catal. B Environ.* **2024**, *342*, 123365.
(24) Chen, X.; Chen, N.; Fang, G.; Wang, Y. Mechanism of Sulfite-Enhanced As(III) Oxidation in As(III)-Fe Minerals under Ambient Conditions. *J. Hazard. Mater.* **2024**, *465*, 133292.
(25) Cheng, B.; Zhan, H.; Lu, Y.; Xing, D.; Lv, X.; Frauenheim, T.; Zhou, P.; Wang, S.; Zou, Y. Oxygen Defect Site Filling Strategy Induced Moderate Enrichment of Reactants for Efficient Electrocatalytic Biomass Upgrading. *Adv. Sci.* **2024**, *11* (48), 2410725.
(26) Zhao, Z.; Jia, Y.; Xu, L.; Zhao, S. Adsorption and Heterogeneous Oxidation of As(III) on Ferrihydrite. *Water Res.* **2011**, *45* (19), 6496−6504.
(27) Greenleaf, J. E.; Cumbal, L.; Staina, I.; Sengupta, A. K. Abiotic As(III) Oxidation by Hydrated Fe(III) Oxide (HFO) Microparticles in a Plug Flow Columnar Configuration. *Process Saf. Environ. Prot.* **2003**, *81* (2), 87−98.
(28) Liu, X.; Li, Z.; Jin, L.; Wang, H.; Huang, Y.; Huang, D.; Liu, X. Peracetic Acid Activation by Modified Hematite for Water Purification: Performance, Degradation Pathways, and Mechanism. *Langmuir* **2024**, *40* (29), 15301−15309.
(29) Catalano, J. G.; Fenter, P.; Park, C.; Zhang, Z.; Rosso, K. M. Structure and Oxidation State of Hematite Surfaces Reacted with Aqueous Fe(II) at Acidic and Neutral pH. *Geochim. Cosmochim. Acta* **2010**, *74* (5), 1498−1512.
(30) Rosso, K. M.; Yanina, S. V.; Gorski, C. A.; Larese-Casanova, P.; Scherer, M. M. Connecting Observations of Hematite (α-Fe_2O_3) Growth Catalyzed by Fe(II). *Environ. Sci. Technol.* **2010**, *44* (1), 61−67.
(31) Frierdich, A. J.; Helgeson, M.; Liu, C.; Wang, C.; Rosso, K. M.; Scherer, M. M. Iron Atom Exchange between Hematite and Aqueous Fe(II). *Environ. Sci. Technol.* **2015**, *49* (14), 8479−8486.
(32) Jia, Q. Q.; Zhang, X.; Deng, J.; Huang, L. Z. Labile Fe(III) Phase Mediates Electron Transfer from Fe(II,III) (Oxyhydr)Oxides to Carbon Tetrachloride. *Water Res.* **2023**, *245*, 120636.
(33) Sheng, A.; Liu, J.; Li, X.; Qafoku, O.; Collins, R. N.; Jones, A. M.; Pearce, C. I.; Wang, C.; Ni, J.; Lu, A.; Rosso, K. M. Labile Fe(III) from Sorbed Fe(II) Oxidation Is the Key Intermediate in Fe(II)-Catalyzed Ferrihydrite Transformation. *Geochim. Cosmochim. Acta* **2020**, *272*, 105−120.
(34) Lemine, O. M.; Sajieddine, M.; Bououdina, M.; Msalam, R.; Mufti, S.; Alyamani, A. Rietveld Analysis and Mössbauer Spectroscopy Studies of Nanocrystalline Hematite (α-Fe_2O_3). *J. Alloys Compd.* **2010**, *502* (2), 279−282.
(35) Larese-Casanova, P.; Scherer, M. M. Morin Transition Suppression in Polycrystalline ^{57}Hematite (α-Fe_2O_3) Exposed to Fe(II). *Hyperfine Interact.* **2007**, *174* (1), 111−119.
(36) Berquó, T. S.; Imbernon, R. A. L.; Blot, A.; Franco, D. R.; Toledo, M. C. M.; Partiti, C. S. M. Low-Temperature Magnetism and Mössbauer Spectroscopy Study of Natural Goethite. *Phys. Chem. Miner.* **2007**, *34* (5), 287−294.
(37) Luan, F.; Gorski, C. A.; Burgos, W. D. Thermodynamic Controls on the Microbial Reduction of Iron-Bearing Nontronite and Uranium. *Environ. Sci. Technol.* **2014**, *48* (5), 2750−2758.
(38) Wan, C. T. C.; Ismail, A.; Quinn, A. H.; Chiang, Y. M.; Brushett, F. R. Synthesis and Characterization of Dense Carbon Films as Model Surfaces to Estimate Electron Transfer Kinetics on Redox Flow Battery Electrodes. *Langmuir* **2023**, *39* (3), 1198−1214.
(39) Pak, J.; Chang, W.; Kwon, C. H.; Cho, J. Recent Advances in Enzyme-Based Biofuel Cells Using Glucose Fuel: Achieving High Power Output and Enhanced Operational Stability. *Adv. Funct. Mater.* **2025**, *35* (16), 2415933.
(40) Zhang, S.; Lyu, X.; Torres, C. H.; Darwish, N.; Ciampi, S. Non-Ideal Cyclic Voltammetry of Redox Monolayers on Silicon Electrodes: Peak Splitting is Caused by Heterogeneous Photocurrents and Not by Molecular Disorder. *Langmuir* **2022**, *38* (2), 743−750.
(41) El-Latif, E. I. A.; Kebede, M. A.; Sekar, K.; Hameed, T. A.; Yahia, I. S.; Gao, H.; Sheha, E. Modeling the Diffusion Coefficient of Charge Carriers in Metal Ion Batteries Using the Randles-Sevcik Equation. *Adv. Theory Simul.* **2025**, *8* (8), 2500346.

Downloaded from pubs.acs.org/langd5/article-pdf/42/26/19343/6521356l/acs.langmuir.6c02392.pdf by UNIV TUEBINGEN user on 17 September 2026

https://doi.org/10.1021/acs.langmuir.6c02392
Langmuir 2026, 42, 19343−19353

(42) Pervez, S.; Iqbal, M. Z. Capacitive and Diffusive Contributions in Supercapacitors and Batteries: A Critique of b-Value and the $\nu-\nu^{1/2}$ Model. *Small* **2023**, *19* (48), 2305059.
(43) Ubbink, R. F.; Gudjonsdottir, S.; Vogel, Y. B.; Houtepen, A. J. Numerical Model to Simulate Electrochemical Charging of Nanocrystal Films. *J. Phys. Chem. C* **2023**, *127* (20), 9896−9902.
(44) Lin, F.; Chen, Z.; Gong, H.; Wang, X.; Chen, L.; Yu, H. Oxygen Vacancy Induced Strong Metal-Support Interactions on Ni/$Ce_{0.8}Zr_{0.2}O_2$ Nanorod Catalysts for Promoting Steam Reforming of Toluene: Experimental and Computational Studies. *Langmuir* **2023**, *39* (12), 4495−4506.

Downloaded from pubs.acs.org/langd5/article-pdf/42/26/19343/6521356l/acs.langmuir.6c02392.pdf by UNIV TUEBINGEN user on 17 September 2026

https://doi.org/10.1021/acs.langmuir.6c02392
Langmuir 2026, 42, 19343−19353